Chinese Journal of Structural Chemistry

ARTICLE

Ultrathin $ZnIn_2S_4$ Nanosheets-Supported Metallic Ni_3FeN for Photocatalytic Coupled Selective Alcohol Oxidation and H_2 Evolution

Mengqing Li[1], Weiliang Qi[2], Jiuyang Yu[2], Lijuan Shen[1], Xuhui Yang[1], Siqi Liu[2]* and Min-Quan Yang[1]*

[1]*College of Environmental Science and Engineering, Fujian Key Laboratory of Pollution Control & Resource Reuse, Fujian Normal University, Fuzhou 350007, China*

[2]*School of Environmental Science and Technology, Dalian University of Technology, Dalian 116024, China*

ABSTRACT Photocatalytic anaerobic organic oxidation coupled with H_2 evolution represents an advanced solar energy utilization strategy for the coproduction of clean fuel and fine chemicals. To achieve a high conversion efficiency, the smart design of efficient catalysts by the right combination of semiconductor light harvesters and cocatalyst is highly required. Herein, we report a composite photocatalyst composed of noble metal-free transition metal nitride Ni_3FeN decorated on 2D ultrathin $ZnIn_2S_4$ (ZIS) nanosheets for selective oxidation of aromatic alcohols to aldehydes pairing with H_2 production. In the composite, ultrathin ZIS serves as a light harvester that greatly shortens the diffusion length of photogenerated charges, while the metallic nitride Ni_3FeN acts as an advanced cocatalyst which not only captures the photoelectrons generated from the ultrathin ZIS to promote the charge separation, but also provides active sites to lower the overpotential and accelerate the H_2 reduction. The best photocatalytic performance is found on ZIS/1.5% M-Ni_3FeN, which shows a H_2 generation rate of 2427.9 μmol g^{-1} h^{-1} and a benzaldehyde (BAD) production rate of 2460 μmol g^{-1} h^{-1}, about 7.8-fold as high as that of bare ZIS. This work is anticipated to endorse the exploration of transition metal nitrides as high-performance cocatalysts to promote the coupled photocatalytic organic transformation and H_2 production.

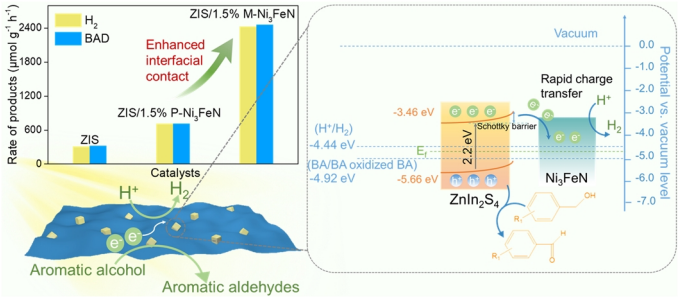

Keywords: transition metal nitrides, cocatalyst, ultrathin 2D nanosheets, electrostatic self-assembly, interfacial contact, selective alcohol oxidation, H_2 evolution

n INTRODUCTION

The fast exhaustion of fossil fuels and deterioration of environment urgently call for the excavation of new renewable energy resources. Solar-driven photocatalytic H_2 evolution has long been deemed as an appealing approach to assure sustainable energy supply and achieve a carbon-neutral society.[1-8] However, the typical strategy of photocatalytic overall water splitting generally suffers from a low H_2 production rate due to the sluggish water oxidation kinetics, while the photocatalytic H_2 evolution half reaction is essentially restricted by the use of sacrificial agent, which wastes the oxidizing power of the excited holes and raises the reaction cost.[9] In this context, the emerging approach of coupling photocatalytic H_2 evolution with organic transformations, in which the oxidation of water or sacrifice agent is replaced by the selective oxidation of organics, provides an advanced alternative approach to tackle the challenges.[10-15] To scale up the scheme, the design of high-efficient photocatalysts with excellent optoelectronic properties to allow both efficient capture of solar light and separation of photoexcited charge carriers is a focused task.

Over the past decade, tremendous efforts have been devoted to the design and synthesis of ultrathin two-dimensional (2D) catalysts dictated by their distinctive physical-chemical properties different from bulk counterparts. Specifically, the 2D photocatalysts have been revealed with desirable features such as high specific surface area, short charge diffusion length, and fast charge mobility.[16-18] Among diverse promising candidates, $ZnIn_2S_4$ (ZIS) is recognized as an outstanding material due to its intrinsic 2D structure, suitable bandgap, favorable chemical stability, and excellent visible light absorption properties.[19-22] Nevertheless, the photoactivity of single component ZIS is still retarded by the undesirable surface charge recombination and lack of surface redox reaction sites.[23]

To ameliorate the limitation, cocatalyst loading onto semiconductor surface is one of the most effective means, which can not only provide a large amount of reactive sites but also capture the electrons generated from the semiconductor.[24-28] Traditionally, noble metals (*e.g.*, Pt, Pd, Au, Ru) are widely selected, but they suffer from resource scarcity and high cost.[20,29-31] Plenty of researches have been dedicated to exploring noble-metal-free materials.[32-37] Transition metal nitrides (TMNs) are a kind of metallic interstitial compounds fabricated by inserting nitrogen atoms into metal lattice. The introduction of nitrogen atoms expands the crystal lattice and rearranges the density of states (DOS) near the Fermi level of the metal. Therefore, the TMNs possess electronic structures similar to that of noble metals, which are highly desirable for acting as advanced cocatalyst.[38-41] However, to date, the application of TMNs for the photocatalytic coupled reaction of organic transformation and H_2 evolution is still sparse.

Herein, we present the design and fabrication of a new ZIS/Ni_3FeN composite photocatalyst for efficient selective oxidation of aromatic alcohols to aldehydes along with the production

DOI: 10.14102/j.cnki.0254-5861.2022-0147

of H_2. Bimetallic nitrides Ni_3FeN are integrated with ultrathin 2D ZIS nanosheets via a facile electrostatic self-assembly method, which forms well contacted heterointerface. A H_2 production rate of 2427.9 μmol h^{-1} g^{-1} and a benzaldehyde selectivity of 99% are obtained over the optimal ZIS/Ni_3FeN sample, which is about 7.8-folds as high as that of bare ZIS. On the basis of collective spectroscopic and photoelectrochemical measurements, the higher photocatalytic performance of the hybrid ZIS/Ni_3FeN composite than bare ZIS is majorly owing to that the Ni_3FeN efficiently captures electrons from ZIS and accelerates the surface H_2 reduction rates. The study demonstrates the great potential of transition metal nitrides as highly efficient cocatalysts for selective oxidation of aromatic alcohols into corresponding aldehydes coupled with H_2 evolution.

n RESULTS AND DISCUSSION

The synthesis of the hybrid ZIS/M-Ni_3FeN composite is realized by an electrostatic self-assembly method, as schematically illustrated in Figure 1a. Based on Zeta potential analysis, the surface charge modification has shown important influence on the interfacial interaction of ZIS/M-Ni_3FeN. As revealed in Figure S1, both of the pristine Ni_3FeN and ZIS show negative surface charge, which is difficult to form a good interface contact between them due to the electrostatic repulsion. As such, to optimize the interfacial interaction, Ni_3FeN has been modified with surfactant APTES (marked as M-Ni_3FeN) to endow it with positive charge (Figure S2). After surface modification, the positive M-Ni_3FeN can spontaneously and strongly assemble onto the ZIS nanosheets by simply dropwise adding the M-Ni_3FeN dispersion into the aqueous solution of ZIS.[42] This simple solution-based assembly method avoids high-energy input procedures and complex process control, which is easy to be scaled up for large-scale preparation. Moreover, the method also enables the facile modulation of constituent ratio to optimize the photocatalytic activity of the hybrid composites.

The morphological structures of the synthesized samples were firstly analyzed by scanning electron microscopy (SEM) analysis. As displayed in Figure S3a, the bare ZIS shows a uniform flake-like morphology. Transmission electron microscopy (TEM) image of the nanosheets shows transparent feature, denoting an ultrathin thickness of the ZIS (Figure S4). Additionally, atomic force microscope (AFM) further reveals the thickness of the nanosheet is around 2.7 nm (Figure S3b), which proves a single-unit-cell structure of ZIS. The ultrathin structure enables an immediate transfer of photogenerated charge carriers to the surface after photoexcitation, which would greatly inhibit the bulk charge recombination. For Ni_3FeN, the SEM analysis shows uniform particle morphology with diameters of approximately 125 nm (Figure S5). After APTES modification, no perceptible influence on the morphology of M-Ni_3FeN is detected (Figure S6). Figure 1b shows the SEM image of ZIS/M-Ni_3FeN, which discloses that Ni_3FeN nanoparticles are attached onto the surface of ZIS. More structural information of the composite is obtained via TEM and high-resolution TEM (HRTEM) analysis. As depicted in Figure 1c, obviously, the Ni_3FeN nanoparticles are intimately loaded on the surfaces of ZIS nanosheets, which is consistent with the SEM image. The HRTEM image (Figure 1d-e) of the ZIS/M-Ni_3FeN composite reveals two lattice fringes. The lattice stripe of 0.32 nm can be indexed to the (102) plane of ZIS, while another lattice spacing of 0.22 nm matches with the (111) crystal facet of Ni_3FeN.[38,43] The intersecting of ZIS and Ni_3FeN confirms the formation of a closely contacted interface, which would benefit the transfer of photoexcited electrons from ZIS to Ni_3FeN.

To reveal the chemical element compositions and valence states of the composite, X-ray photoelectron spectroscopy (XPS) measurement is carried out. As manifested in Figure 2a, for Zn 2p spectrum, two characteristic peaks with binding energies of 1021.9 and 1044.9 eV are detected, which belong to the Zn $2p_{3/2}$ and Zn $2p_{1/2}$ of Zn^{2+}, respectively.[44] The In 3d spectrum of ZIS/M-Ni_3FeN can be divided into In $3d_{3/2}$ (452.5 eV) and In $3d_{5/2}$ (444.9 eV) regions (Figure 2b), corresponding to the In^{3+}.[45] The two peaks of S 2p located at 162.9 eV (S $2p_{1/2}$) and 161.6 eV (S $2p_{3/2}$) are matched with S^{2-} (Figure 2c).[46] Meanwhile, in the Ni 2p region (Figure 2d), the peaks at 852.7 and 869.9 eV are related to metallic nickel (Ni^0), while the binding energies of 855.9 and 873.4 eV are fitted into $2p_{3/2}$ and $2p_{1/2}$ of Ni^{2+}, respectively.[47] The satellite peaks are located at 861.7 and 879.9 eV. In the XPS pattern of Fe 2p (Figure 2e), the binding energies positioned at about 707.1 and 719.5 eV can be attributed to Fe^0. The peaks of 711.5 and 724.5 eV can be assigned to Fe^{3+}.[48] Another two satellite peaks are observed at 716.1 and 732.3 eV. The states of Ni^{2+} and Fe^{3+} around the surface of composite are caused by inevitable surface oxidation of Ni_3FeN exposed to air.[38,49] As for the N 1s spectrum, it can be divided into four peaks at 396.2, 397.4, 398.7,

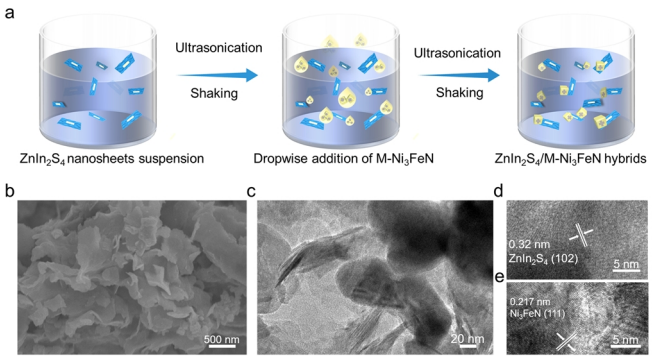

Figure 1. (a) Schematic illustration for the synthesis of ZIS/M-Ni_3FeN hybrids. (b) SEM, (c) TEM and (d-e) HRTEM of ZIS/M-Ni_3FeN composite.

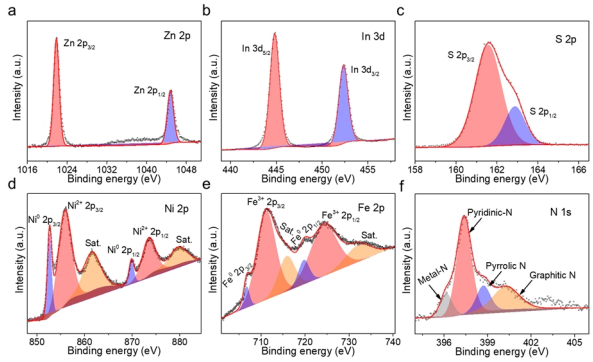

Figure 2. XPS spectra of (a) Zn 2p, (b) In 3d, (c) S 2p, (d) Ni 2p, (e) Fe 2p and (f) N 1S of ZIS/M-Ni_3FeN composite.

Chin. J. Struct. Chem. **2022**, 41, 2212015-2212024
DOI: 10.14102/j.cnki.0254-5861.2022-0147

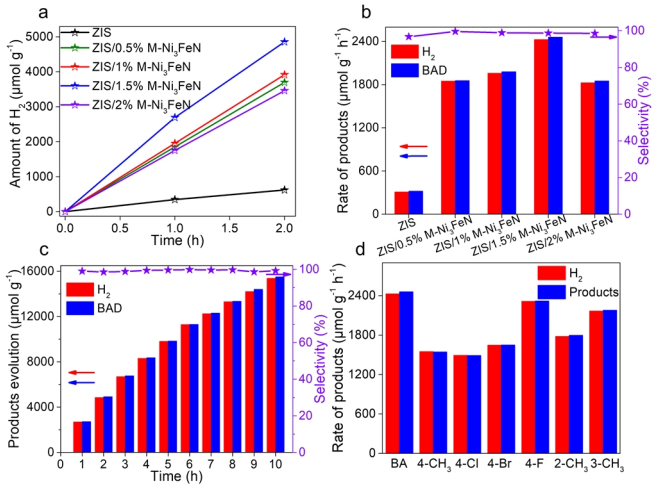

Figure 3. (a,b) Photocatalytic anaerobic oxidation of benzyl alcohol to benzaldehyde and H_2 over different ZIS/M-Ni_3FeN composites. (c) Long-term photoactivity test over ZIS/1.5% M-Ni_3FeN. (d) Photocatalytic performance of ZIS/1.5% M-Ni_3FeN for anaerobic oxidation of different aromatic alcohols.

and 400.4 eV, corresponding to the metal-N, pyridine-N, pyrrole N, and graphitic-N, respectively (Figure 2f).[50,51] Based on the above analysis, the successful synthesis of ZIS/M-Ni_3FeN composite is further confirmed.

To verify the effectiveness of catalysts, the photocatalytic activity of ZIS/M-Ni_3FeN hybrids has been estimated by visible-light-driven selective alcohol oxidation integrated with H_2 evolution under anaerobic condition. Figure 3a-b show the H_2 evolution and benzaldehyde (BAD) formation rates from anaerobic oxidation of BA over ZIS/M-Ni_3FeN with different weight percentages of M-Ni_3FeN. The bare ZIS exhibits a quite low photoactivity (H_2 production rate of 309 μmol g^{-1} h^{-1} and BAD generation rate of 320 μmol g^{-1} h^{-1}), which should be ascribed to the surface charge recombination and insufficient surface redox reaction sites of the bare ZIS. In addition, no H_2 is produced for pristine Ni_3FeN under visible light irradiation because of its metallic characteristic. After the integration of M-Ni_3FeN with ZIS, the hybrid composites reveal markedly enhanced photocatalytic performance. Thus, Ni_3FeN mainly acts as an efficient cocatalyst to boost the photoredox reaction in the ZIS/M-Ni_3FeN composite. The best photocatalytic performance is found on ZIS/1.5% M-Ni_3FeN, which shows a H_2 evolution rate of 2427.9 μmol g^{-1} h^{-1} and a BAD generation rate of 2460 μmol g^{-1} h^{-1}, approximately 7.8 times higher than that of bare ZIS. The yield ratios of BAD and H_2 are close to 1:1, indicating a high selectivity of BAD generation.

Moreover, the apparent quantum efficiency (AQE) of ZIS/1.5% M-Ni_3FeN composite at 420 nm is calculated to be 8.6% (Figure S7), which is comparable to that of the recently reported state-of-the-art photocatalyst systems for the coupled selective alcohol oxidation and H_2 evolution (Table 2), further indicating high-performance of the ZIS/M-Ni_3FeN composite. Notably, the weight ratio of M-Ni_3FeN shows important effect on the photocatalytic performance. By varying the addition ratio of M-Ni_3FeN, the photocatalytic activities of the composites show a volcano-type trend, which can be ascribed to that at a low mass percentage, the lack of M-Ni_3FeN species leads to insufficient surface active sites. On the contrary, excessive addition of M-Ni_3FeN will cause an agglomeration of the nanoparticles, and induce a shading effect that blocks the visible light absorption of ZIS, thus depressing the photoactivities of the composites.[52]

Moreover, the stability of ZIS/M-Ni_3FeN composite has been examined through a long-term experiment. As can be seen from Figure 3c, taking the optimal ZIS/1.5% M-Ni_3FeN as an example, the sample retains stable photocatalytic H_2 evolution over a 10 h visible light irradiation, and the selectivity of BAD reaches up to 99% after the reaction test. The XPS and SEM analyses reveal that the chemical states and morphology of Ni_3FeN in the used composite are almost unchanged in comparison with those in the fresh sample (Figures S8 and S9). Furthermore, the cyclic test of the ZIS/1.5% M-Ni_3FeN composite has also been performed. As displayed in Figure S10, no apparent performance degradation is detected during the six recycle tests. These results validate high stability of the metallic Ni_3FeN and ZIS/M-Ni_3FeN composite for photocatalytic H_2 evolution coupled with organic transformation.

To study the general applicability of ZIS/M-Ni_3FeN composite, the photocatalytic anaerobic oxidation of a series of aromatic alcohols that contain different substituent groups is tested under the same conditions. As presented in Figure 3d, it is obvious that for diverse aromatic alcohols, including 4-methylbenzyl alcohol, 4-fluorobenzyl alcohol, 4-chlorobenzyl alcohol, 4-bromobenzyl alcohol, 2-methylbenzyl alcohol and 3-methylbenzyl alcohol, the ZIS/M-Ni_3FeN can realize simultaneous H_2 evolution and aldehyde production. The result manifests that the ZIS/M-Ni_3FeN composite is universal towards the photocatalytic anaerobic oxidation of different aromatic alcohols.

In order to illustrate the importance of interfacial interaction induced by surface modification on the photoactivity of the ZIS/M-Ni_3FeN composite, a series of ZIS/P-Ni_3FeN comparison samples with the same weight ratios of Ni_3FeN have also been synthesized. The process is similar to the preparation of ZIS/M-Ni_3FeN composite except that the Ni_3FeN is used without APTES modification. As shown in Figure S11, typical structures of $NiFe_3N$ particle and ZIS nanosheets are observed in the SEM image, and the $NiFe_3N$ particles are wrapped by the ZIS nanosheets. However, it is notable that abundant Ni_3FeN particles are aggregated into large agglomerate in the hybrid composite, which are separated from the ZIS nanosheets, implying an insufficient interfacial contact between the two components.

Thereafter, the photocatalytic activity of ZIS/P-Ni_3FeN hybrids in different proportions has been tested under the same experimental conditions. As illustrated in Figure S12, the ZIS/P-Ni_3FeN hybrids show increased photocatalytic activities as compared with bare ZIS, indicating the simple mixture of Ni_3FeN can also effectively enhance the photoactivity of ZIS. Nevertheless, the photocatalytic performance for all of the ZIS/P-Ni_3FeN composites is much lower than that of the ZIS/M-Ni_3FeN hybrid, which are synthesized with different interfacial contact. The optimum photocatalytic H_2 evolution rate and BAD production rate obtained over the ZIS/1.5% P-Ni_3FeN hybrid are 704 μmol g^{-1} h^{-1} and 712.5 mmol g^{-1} h^{-1}, respectively. The photoactivity is only a quarter of the

DOI: 10.14102/j.cnki.0254-5861.2022-0147

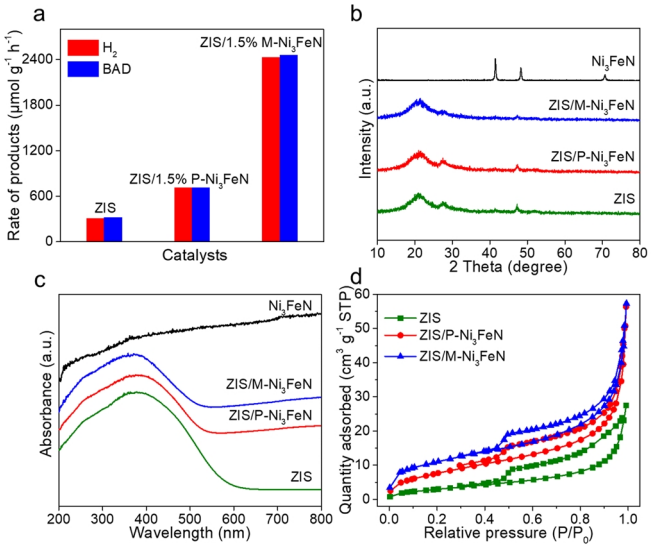

with H_2 evolution over ZIS, ZIS/1.5% P-Ni_3FeN and ZIS/1.5% M-Ni_3FeN hybrids. (b) XRD patterns, (c) DRS spectra and (d) N_2 adsorption-desorption isotherms.

$ZnIn_2S_4$/1.5% M-Ni_3FeN sample with the same content of Ni_3FeN (Figure 4a). The results highlight the importance of enhancing interfacial contact for fabricating advanced hybrid composites. The significantly decreased photoactivity might result from the weak interaction between the Ni_3FeN and ZIS nanosheets caused by their electrostatic repulsion with the same negative surface charge, which results in insufficient interfacial charge transfer and lower surface reaction rates. This has been verified in the following collective physicochemical and photoelectrochemical characterizations.

Figure 4b shows the X-ray diffraction (XRD) patterns of the bare ZIS, Ni_3FeN, ZIS/P-Ni_3FeN and ZIS/M-Ni_3FeN hybrid composites, which are characterized to study the crystal structures and phase composition of the samples. The three samples of ZIS, ZIS/P-Ni_3FeN and ZIS/M-Ni_3FeN display similar diffraction peaks at around 21.6°, 27.7°, 30.8°, 39.4°, 47.3°, 52.4° and 55.6° that are well indexed to a bare hexagonal $ZnIn_2S_4$ structure (standard card, JCPDS No. 65-2023).[53] There is no phase change of $ZnIn_2S_4$ or generation of new component during the synthesis process after loading P-Ni_3FeN and M-Ni_3FeN due to that the assembly synthesis was operated under low temperature. In addition, the ZIS/M-Ni_3FeN with different addition ratios of Ni_3FeN exhibits similar XRD patterns, which are the same as that of ZIS (Figure S13). No characteristic diffraction peaks corresponding to Ni_3FeN are detected in XRD patterns (Figure S14) for all the ZIS/M-Ni_3FeN composite, which is inferred to be caused by the low content of Ni_3FeN.[38] The above analyses reveal that the integration with Ni_3FeN and the APTES modification of Ni_3FeN both have negligible effect on the chemical properties of ZIS. The well-maintained crystal structures of ZIS and Ni_3FeN in the composites enable the study of different interfacial effects on the photocatalytic performance and simplifies the identification of respective roles of each component in the composite.

The optical absorption properties of the samples have been measured by UV-vis diffuse reflectance spectroscopy (DRS), as displayed in Figure 4c. It is apparent that bare ZIS shows strong optical absorption in the visible light region and possesses an absorption edge at about 550 nm. Due to the metallic character of pristine Ni_3FeN, a strong absorption at 200-800 nm appears.[54] After integrating with M-Ni_3FeN, the visible light absorption of ZIS/M-Ni_3FeN composite shows an enhancement of visible light absorption in the range of 550-800 nm. Similar light absorption enhancement is observed in ZIS/P-Ni_3FeN, which is caused by the inherent background absorption of black-colored Ni_3FeN.[55] With the increase of M-Ni_3FeN contents in the samples, the absorbance of visible light also gradually rises (Figure S15), which coincides with the color change of the composites. Moreover, the band gaps (E_g) of the samples have been calculated according to the Tauc plot.[56,57] Figure S16 indicates that the band gaps of bare ZIS, ZIS/P-Ni_3FeN and ZIS/M-Ni_3FeN hybrid are about 2.2, 2.3 and 2.33 eV, respectively. The combination of Ni_3FeN with ZIS increases the band gaps of ZIS/Ni_3FeN, which can be ascribed to the quantum confinement effect induced by the inhibited agglomeration of nanosheets in the composites.[58]

To further study the microstructure, Brunauer-Emmett-Teller (BET) surface area, pore size distribution, and pore volume of the samples have been analyzed by N_2 adsorption-desorption measurement. All the three samples show characteristic type IV isotherms with a H3 hysteresis loop (Figure 4d), illustrating the presence of a mesoporous structure.[59] This has also been proven by the pore diameter distribution curves (Figure S17). Moreover, the specific surface areas of bare ZIS, ZIS/P-Ni_3FeN and ZIS/M-Ni_3FeN are 11.59, 27.39 and 35.34 $m^2 g^{-1}$, respectively (Table S1). The increased BET surface area of ZIS/Ni_3FeN also indicates the prohibited agglomeration of ZIS nanosheets after the introduction of Ni_3FeN. In addition, the BET surface area of ZIS/M-Ni_3FeN is higher than that of ZIS/P-Ni_3FeN, indicating that the better dispersity of M-Ni_3FeN expands the contact area between M-Ni_3FeN and ZIS, thus further effectively impeding the agglomeration of ultrathin ZIS nanosheets and enlarging the surface area of the composites. Generally, a large surface area is in favor of enhancing the interfacial contact between the photocatalyst and reactant, exposing more surface active sites and improving the migration rate of photoexcited charge carrier, which could be contributed to enhancing the photoactivity.[60]

To explore the effect of Ni_3FeN in promoting the interfacial charge separation and transfer, a series of photoelectrochemical tests have been carried out. The transient photocurrent responses are measured by several on-off intermittent cycles under visible light irradiation, as shown in Figure 5a. The photocurrent responses of photocatalysts are proportional to the separation efficiency of interfacial charge.[61,62] It can be seen that all samples display a relatively stable light response and the photocurrent density is in an order of ZIS/M-Ni_3FeN > ZIS/P-Ni_3FeN > ZIS under an identical experimental condition. The ZIS/M-Ni_3FeN exhibits the highest photocurrent intensity, indicating that the integration with M-Ni_3FeN most effectively promotes the separation and transfer of photogenerated electron-hole pairs of ZIS.[63-66] The optimized charge separation has been further confirmed by the electrochemical impedance spectroscopy (EIS) measurement.

Chin. J. Struct. Chem. **2022**, 41, 2212015-2212024
DOI: 10.14102/j.cnki.0254-5861.2022-0147

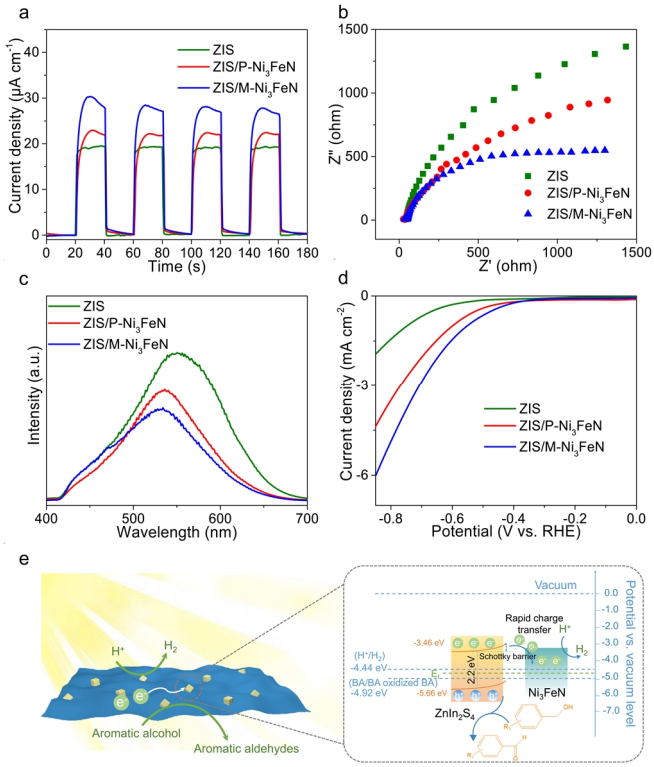

Figure 5. (a) Transient photocurrent response. (b) EIS Nyquist plots. (c) Steady-state PL spectra and (d) LSV curves. (e) A mechanism for photocatalytic H_2 evolution coupling with aldehydes production over ZIS/M-Ni_3FeN hybrids.

Ni_3FeN shows a small semicircle diameter of the Nyquist plot (Figure S18a). Moreover, as shown in Figure 5b, compared with ZIS and ZIS/P-Ni_3FeN, the ZIS/M-Ni_3FeN exhibits the smallest semicircle diameter of the Nyquist plot, confirming the lowest resistance and highest charge transfer efficiency between the ZIS/M-Ni_3FeN electrode and electrolyte solution, which is beneficial for inhibiting the charge combination of the photocatalyst and hence improves the photocatalytic property.[67,68] The enhanced electrical conductivity of the composites can be mainly ascribed to the introduction of Ni_3FeN with intrinsic metallic conductivity.

The steady-state photoluminescence (PL) spectroscopy is also carried out to verify the increased charge-carrier separation and transfer efficiency. The PL intensity reflects the recombination of photoexcited electron-hole pairs.[69] Figure 5c shows that bare ZIS presents a broad PL emission peak at around 550 nm. In comparison, the emission peaks for ZIS/M-Ni_3FeN and ZIS/P-Ni_3FeN composites are notably quenched, denoting that the combination of Ni_3FeN with ZIS effectively suppresses the recombination of charge carriers. The lower PL signal of ZIS/M-Ni_3FeN than ZIS/P-Ni_3FeN can be attributed to the more efficient interfacial contact in the composite, which leads to faster electron transfer from photoexcited ZIS to Ni_3FeN.[70-72] To further study the electron transfer behavior in the composite, the transient PL spectrum has been tested. As presented in Figure S19, the fluorescence lifetime of ZIS/M-Ni_3FeN (0.17 ns) and ZIS/P-Ni_3FeN (0.52 ns) is shorter than that of ZIS (0.74 ns), implying the formation of an electron transfer pathway from ZIS to Ni_3FeN in a non-radiative quenching manner.[8,73] The Ni_3FeN as a cocatalyst could effectively receive photogenerated charge carriers to inhibit the surface charge recombination. Notably, compared with ZIS/P-Ni_3FeN, the apparent lifetime diminution of ZIS/M-Ni_3FeN could be attributed to the better interfacial contact of ZIS/M-Ni_3FeN, which more efficiently promotes the charge carrier migration from ZIS to Ni_3FeN. The result is consistent with the PL quenching test.

Moreover, to confirm that the Ni_3FeN can provide active site to promote surface H_2 evolution reaction, the proton reduction activities of ZIS, ZIS/P-Ni_3FeN and ZIS/M-Ni_3FeN are investigated by the linear sweep voltammetry (LSV) approach. As shown in Figure 5d, the cathodic current observed in the range of 0 to -0.85 V (vs. NHE) can be attributed to H_2 evolution. The bare ZIS exhibits a low reduction current due to the lack of enough active sites. On the contrary, Ni_3FeN shows a strong reduction current under the same condition (Figure S18b). The obviously higher current density of ZIS/Ni_3FeN than that of bare ZIS at the same potential range demonstrates that the loading of Ni_3FeN can efficiently capture the electrons and facilitate the reduction of protons to H_2. Especially, ZIS/M-Ni_3FeN shows a much higher reduction current, illustrating that the combination with M-Ni_3FeN optimizes the proton reduction ability of the composites.[74,75]

To better elucidate the photocatalytic mechanism, gas chromatography-mass (GC-MS) and EPR measurements have been tested. As shown in Figure S20, three peaks are detected for the reaction solution after light irradiation of 1 h, which belongs to the solvent of acetonitrile, product of benzaldehyde and reactant of benzyl alcohol, respectively. The absence of other products and intermediates denotes the high selectivity of the reaction. Moreover, the EPR measurement has been performed using 5,5-dimethyl-1-pyrroline N-oxide (DMPO) as a radical trapping reagent in acetonitrile solvent containing BA under Ar atmosphere. It is obvious that no free radical signals are detected in dark (Figure S21). After the visible light illumination, six characteristic signals are displayed in the EPR spectra of bare ZIS, which prove the generation of a carbon-centered radical.[76,77] However, it is unable to carry out the EPR test over the ZIS/M-Ni_3FeN composite due to its strong magnetism, as presented in Figure S22, which makes it incapable to detect the radical intermediate. In addition, the photoactivity test of ZIS/M-Ni_3FeN in the presence of DMPO as a radical scavenger has been carried out. As displayed in Figure S23, the photocatalytic performance decreased significantly. Based on these results, it can be inferred that the carbon-centered radical is the key intermediate in the photocatalytic process.

To further study the photocatalytic charge transfer in ZIS/Ni_3FeN, the band structures and work functions of ZIS and Ni_3FeN are analyzed. In our previous work, the band structure of ZIS nanosheets has been investigated. The conduction band (CB) and valence band (VB) of ZIS are determined to be around -0.98 V and 1.22 V vs. reversible hydrogen electrode (RHE), respectively. Accordingly, the CB and VB values of ZIS vs. vacuum level are calculated to be -3.46 and -5.66 eV based on the equation of E_{vac} = -4.44 - E_{RHE}.[23,78,79] Moreover, the work function (Φ) and Fermi level (E_f) of Ni_3FeN are determined by density functional theory (DFT) calculation. As displayed in Figure S24, Φ of Ni_3FeN is theo-

DOI: 10.14102/j.cnki.0254-5861.2022-0147

retically calculated to be about 4.97 eV (vs. vacuum level). As such, the E_f of Ni_3FeN is determined to be -4.97 eV (vs. vacuum level) according to the equation of E_f (vs. vacuum level) = E_{vac} - Φ, where E_{vac} is assumed as 0 eV.[80] Based on literature reports, the Φ of ZIS is 4.75 eV (vs. vacuum level) and the corresponding E_f is calculated to be -4.75 eV (vs. vacuum level).[60,81] Therefore, a Schottky junction is formed between the metallic Ni_3FeN cocatalyst and the ZIS semiconductor.

In conclusion, resulting from the above-mentioned analyses, a possible photocatalytic reaction mechanism towards the anaerobic oxidation of aromatic alcohols over ZIS/M-Ni_3FeN hybrids is presented. Before contact, the Ni_3FeN has a larger work function than ZIS (Figure S25). As displayed in Figure 5e, when they are in close contact, an energy difference is formed. The electrons in ZIS could spontaneously transfer to Ni_3FeN until E_f reaches equilibrium. The charge migration leads to an upward band bending of ZIS along the side of the Schottky contact as well as the formation of an internal electric field between ZIS and Ni_3FeN. Under visible light irradiation, the photogenerated electrons could transfer from ZIS to Ni_3FeN and suppress the backflow of electrons. Due to that the electron accumulation causes a negative shift of E_f for Ni_3FeN, the E_f of ZIS/Ni_3FeN composite shifts closer to the CB of ZIS. The higher negative potential of E_f corresponds to stronger reduction ability in the composite.[82-84] Then, the isolated photogenerated electrons and holes would promote H_2 evolution and the oxidation of aromatic alcohol, respectively. Consequently, the introduction of Ni_3FeN effectively accelerates the separation and migration of the photogenerated electrons, and improves the photocatalytic activity.

n CONCLUSION

In summary, we report a bimetallic transition metal nitride Ni_3FeN as a novel noble-metal-free cocatalyst for photocatalytic selective anaerobic oxidation of aromatic alcohols to form corresponding aldehydes pairing with H_2 in one redox cycle, which realizes simultaneous utilization of photogenerated electrons and holes. The synthesis of hybrid ZIS/M-Ni_3FeN composite is realized by a simple yet efficient electrostatic self-assembly method, which is easy to be scaled up. The optimal ZIS/M-Ni_3FeN sample achieves a H_2 evolution rate of 2427.9 μmol h^{-1} g^{-1} and a BAD production rate of 2460 μmol g^{-1} h^{-1}, about 7.8-fold as high as that of bare ZIS. Photoelectrochemical characterizations show that Ni_3FeN not only accelerates interfacial charge separation and transfer, but also promotes surface H_2 evolution reaction. Moreover, a comparison study with ZIS/P-Ni_3FeN reveals that the tight interfacial contact and strong coupling effect in the composites are favorable for separating charges and utilizing active sites. The present study offers insight into the development of economical and efficient transition metal nitride cocatalysts to promote photocatalytic activity in solar energy conversion.

n EXPERIMENTAL

Materials and Reagents. All chemicals in the work were analytic grade and used without further purification. Nickel acetate tetrahydrate ($NiC_4H_6O_4·4H_2O$) was purchased from Aladdin Biochemical Technology Co., Ltd. (Shanghai, China). Trisodium citrate dihydrate ($Na_3C_6H_5O_7·2H_2O$) was purchased from Tianjin Kemiou Chemical Reagent Co., Ltd. (Tianjin, China). Zinc acetate dihydrate ($Zn(CH_3COO)_2·2H_2O$), indium chloride tetrahydrate ($InCl_3·4H_2O$), potassium ferricyanide $K_3[Fe(CN)_6]$, 3-aminopropyltriethoxysilane (APTES), thioacetamide (C_2H_5NS), acetonitrile (C_2H_3N), benzyl alcohol ($C_6H_5CH_2OH$), 2-methylbenzyl alcohol ($C_8H_{10}O$), 3-methylbenzyl alcohol ($C_8H_{10}O$), 4-methylbenzyl alcohol ($C_8H_{10}O$), 4-fluorophenyl alcohol (C_7H_7OF), 4-chlorobenzyl alcohol (C_7H_7ClO), 4-bromobenzyl alcohol (C_7H_7OBr), benzaldehyde (C_7H_6O), 2-methylbenzaldehyde (C_8H_8O), 3-methylbenzaldehyde (C_8H_8O), 4-methylbenzaldehyde (C_8H_8O), 4-fluorobenzaldehyde (C_7H_5OF), 4-chlorobenzaldehyde (C_7H_5OCl), and 4-bromobenzaldehyde (C_7H_5OBr) were all obtained from Shanghai Sinopharm Chemical Reagent Co., Ltd. The deionized (DI) water used throughout the experiments was from local sources.

Synthesis of Ultrathin 2D $ZnIn_2S_4$ Nanosheets. Ultrathin 2D $ZnIn_2S_4$ nanosheets were prepared through a facile refluxing method.[43] In a typical experiment, $Zn(CH_3COO)_2·2H_2O$ (0.5 mmol) and $InCl_3·4H_2O$ (1 mmol) were added into 150 mL DI water and stirred for 30 min at room temperature. Then, 3 mmol of thioacetamide (TAA) was added into the above solution. After being stirred for another 30 min, the mixture was maintained at 95 °C for 5 h under stirring. The product was collected by centrifugation and washed with DI water for three times. Finally, the sample was obtained by drying for further use.

Synthesis of Ni_3FeN Nanoparticles. 0.3 g $NiC_4H_6O_4·4H_2O$ and 0.441 g $Na_3C_6H_5O_7·2H_2O$ were dissolved in 40 mL DI water and stirred for 15 min to get a green solution. At the same time, a yellow solution was obtained by dissolving 0.264 g $K_3[Fe(CN)_6]$ in 60 mL DI water under stirring for 15 min. Then the yellow solution was transferred into the green solution rapidly and stirred for 10 min. The liquid was left overnight and filtered to get the precipitates. Subsequently, such precipitates were washed with DI water and ethanol for three times. The powder was dried at room temperature overnight. After that, the dried precursor was transferred into a muffle furnace and heated to 350 °C at a heating rate of 1 °C min^{-1} and maintained for 1 h. The obtained brown-red powder of $NiFeO_x$ was annealed in a NH_3 flow at 400 °C for 20 min, thus obtaining Ni_3FeN. This pristine sample was labeled as P-Ni_3FeN.

Surface Modification of Ni_3FeN. In brief, 25 mg of Ni_3FeN was dispersed in 50 mL ethanol and sonicated for 1 h at room temperature. Then, 0.15 mL of 3-aminopropyltriethoxysilane (APTES) was added into the solution. The mixture was heated at 60 °C for 4 h. After that, the sample was collected by centrifugation, washed twice with ethanol, and re-dispersed in DI water to obtain the APTES-modified Ni_3FeN (marked as M-Ni_3FeN) suspension with the concentration of 1 mg mL^{-1}.

Synthesis of ZIS/M-Ni_3FeN and ZIS/P-Ni_3FeN Hybrids. The ZIS/M-Ni_3FeN hybrids were prepared by slowly dropping the M-Ni_3FeN suspension into the ZIS suspension under ultrasonication for 1 h and shaking for 12 h. Then, the sample was centrifuged, washed with DI water for 3 times, and dried. By simply changing the adding amount of M-Ni_3FeN, a series of ZIS/M-Ni_3FeN composites with 1%, 3%, 5%, 7% and 10% weight ratios of M-Ni_3FeN

Chin. J. Struct. Chem. **2022**, 41, 2212015-2212024
DOI: 10.14102/j.cnki.0254-5861.2022-0147

were obtained. The ZIS/P-Ni_3FeN hybrids were fabricated via the same procedure except that P-Ni_3FeN without APTES modification was used.

Characterizations. The zeta potential measurements of the samples were taken on a Zetasizer Nano ZS (Malvern Panalytical, UK) at room temperature of 298 K. The morphologies of the samples were measured on a Hitachi 8100 scanning electron microscopy (SEM). Transmission electron microscope (TEM) and high-resolution transmission electron microscopy (HRTEM) images were recorded on a JEM-2100F (JEOL). The crystal structures and crystallinity of the catalysts were measured through a Bruker D8 Advance X-ray diffractometer (XRD) operated at 40 kV and 40 mA with Cu Kα radiation in the 2θ range from 10° to 80°. The UV-vis diffuse reflectance spectra (DRS) were recorded on an Agilent CARY-100 spectrophotometer (100% $BaSO_4$ was used as reference). X-ray photoelectron spectroscopy (XPS) spectra were investigated on Thermo Kalpha (Thermo Fisher Scientific) using a monochromatic Al Kα as the X-ray source. All binding energies were calibrated by the C 1s peak at 284.8 eV of surface adventitious carbon. The thickness of nanosheets was measured by atomic force microscope (AFM) (NanoWizard4, Bruker). Photoluminescence (PL) spectra of solid samples were obtained by RF-5301PC (Shimadzu, Japan) and transient PL was recorded by using a FLS920 Fluorescence Spectrometer equipped with a nanosecond hydrogen flash-lamp (nF920). The Brunauer-Emmett-Teller (BET) specific surface area and pore size distribution were characterized using an adsorption analyzer (BELSORP-Mini-II, Bel, Japan). The electron paramagnetic resonance (EPR) measurements were performed by a Magnettech ESR5000 spectrometer. The products were detected by gas chromatography-mass (GC-MS) (Aligent 5977A GC/MSD, USA).

Photocatalytic Activity Tests. Typically, 10 mg of photocatalyst and 0.1 mmol of aromatic alcohol were added into a quartz reactor containing 3 mL CH_3CN. Prior to light irradiation, the mixture was sonicated for 2 min and then purged with argon (Ar) gas for 10 min to remove air. After that, the reactor was irradiated by visible light (λ > 420 nm) with a 300 W Xe lamp (CEL-PF300-T8, Beijing China Education Au-light Co., Ltd). To keep the photocatalyst in suspension status, a continuous magnetic stirrer was applied at the bottom of the reactor. After reaction, the generated H_2 was measured by a gas chromatograph (GC 9790plus, Fu Li, China, TCD detector, Ar as carrier gas) and the liquid products were analyzed by another gas chromatography (GC-2030, Shimadzu, Japan, FID detector, nitrogen as carrier gas) after centrifuging the suspension at 10000 rpm for 3 min.

The conversion efficiency of alcohols and selectivity of aldehydes production were calculated as follows:

$$\text{Conversion (\%)} = 100 \times [(C_0 - C_{\text{alcohol}})/C_0]\%$$
$$\text{Selectivity (\%)} = 100 \times [C_{\text{aldehyde}}/(C_0 - C_{\text{alcohol}})]\%$$

where C_0 is the initial concentration of alcohol, C_{alcohol} and C_{aldehyde} are the concentrations of alcohol and aldehyde measured after illumination for a certain time, respectively.

Photoelectrochemical Measurements. All the photoelectrochemical measurements were measured in a three-electrode cell using a CHI 760E instrument. A Pt plate and Ag/AgCl electrode were employed as the counter electrode (CE) and reference electrode (RE), respectively. The working electrode was prepared as follows: 5 mg of catalyst powder was dispersed in 0.5 mL of N,N-dimethylformamide (DMF) under ultrasonication. Then, the mixed solution was spread onto the conductive surface of FTO glass and then dried in air. The exposed area of the working electrode was 1 cm^2. The electrochemical impedance spectroscopy (EIS) measurement was carried out in 0.1 M KCl aqueous solution containing 0.01 M $K_3[Fe(CN)_6]$. The transient photocurrent was tested in 0.2 M Na_2SO_4 solution using a 300 W Xenon lamp (CEL-PF300-T8, Beijing China Education Au-light Co., Ltd) equipped with a 420 nm cutoff filter (λ > 420 nm). Linear sweep voltammetry (LSV) curves were also examined in 0.2 M Na_2SO_4 solution.

Computational Methods. All calculations were performed by using the density functional theory (DFT) within the Vienna ab initio Simulation Package (VASP). The projector augmented wave (PAW) method, Perdew-Burke-Ernzerhof (PBE) function and generalized gradient approximation (GCA) potential were used for the exchange-correlation effect. A plane-wave cutoff energy of 600 eV, energy difference criteria of 1×10^{-5} eV and Monkhorst-Pack k-mesh of 13 × 13 × 13 for unit cell were used. A vacuum region of 25 was used to separate the interactions between the neighboring cells of slab models.

n ACKNOWLEDGEMENTS

This work is financially supported by the National Natural Science Foundation of China (21905049 and 22178057), Natural Science Foundation of Fujian Province (2020J01201 and 2021J01197), and the Award Program for Minjiang Scholar Professorship. S. Liu thanks the support from the Fundamental Research Funds for the Central Universities (Grant No. DUT21RC(3)114).

n AUTHOR INFORMATION

Corresponding authors. Emails: yangmq@fjnu.edu.cn and liusiqi@dlut.edu.cn

n COMPETING INTERESTS

The authors declare no competing interests.

n ADDITIONAL INFORMATION

Supplementary information is available for this paper at http://manu30.magtech.com.cn/jghx/EN/10.14102/j.cnki.0254-5861.2022-0147

For submission: https://www.editorialmanager.com/cjschem

n REFERENCES

(1) Maeda, K.; Domen, K. Photocatalytic water splitting: recent progress and future challenges. *J. Phys. Chem. Lett.* **2010**, 1, 2655-2661.

(2) Song, H.; Luo, S.; Huang, H.; Deng, B.; Ye, J. Solar-driven hydrogen production: recent advances, challenges, and future perspectives. *ACS Energy Lett.* **2022**, 7, 1043-1065.

(3) Christoforidis, K. C.; Fornasiero, P. Photocatalytic hydrogen production: a rift into the future energy supply. *ChemCatChem* **2017**, 9, 1523-1544.

DOI: 10.14102/j.cnki.0254-5861.2022-0147

(4) Wang, Z.; Zhu, H.; Tu, W.; Zhu, X.; Yao, Y.; Zhou, Y.; Zou, Z. Host/guest nanostructured photoanodes integrated with targeted enhancement strategies for photoelectrochemical water splitting. *Adv. Sci.* **2022**, 9, 2103744.

(5) Jiang, X.; Chen, Y.-X.; Lu, C.-Z. Bio-inspired materials for photocatalytic hydrogen production. *Chin. J. Struct. Chem.* **2020**, 39, 2123-2130.

(6) Zhang, M.; Li, H.; Zhang, J.; Lv, H.; Yang, G.-Y. Research advances of light-driven hydrogen evolution using polyoxometalate-based catalysts. *Chin. J. Catal.* **2021**, 42, 855-871.

(7) Qin, L.; Zhao, C.; Yao, L.-Y.; Dou, H.; Zhang, M.; Xie, J.; Weng, T.-C.; Lv, H.; Yang, G.-Y. Efficient photogeneration of hydrogen boosted by long-lived dye-modified Ir(III) photosensitizers and polyoxometalate catalyst. *CCS Chemistry* **2022**, 4, 259-271.

(8) Zhang, M.; Xin, X.; Feng, Y.; Zhang, J.; Lv, H.; Yang, G.-Y. Coupling Ni-substituted polyoxometalate catalysts with water-soluble CdSe quantum dots for ultraefficient photogeneration of hydrogen under visible light. *Appl. Catal. B: Environ.* **2022**, 303, 120893.

(9) Xue, W.; Chang, W.; Hu, X.; Fan, J.; Liu, E. 2D mesoporous ultrathin $Cd_{0.5}Zn_{0.5}S$ nanosheet: fabrication mechanism and application potential for photocatalytic H_2 evolution. *Chin. J. Catal.* **2021**, 42, 152-163.

(10) Xia, B.; Zhang, Y.; Shi, B.; Ran, J.; Davey, K.; Qiao, S. Z. Photocatalysts for hydrogen evolution coupled with production of value-added chemicals. *Small Methods* **2020**, 4, 2000063.

(11) Qi, M.-Y.; Conte, M.; Anpo, M.; Tang, Z.-R.; Xu, Y.-J. Cooperative coupling of oxidative organic synthesis and hydrogen production over semiconductor-based photocatalysts. *Chem. Rev.* **2021**, 121, 13051-13085.

(12) Wang, J.; Qi, M.-Y.; Wang, X.; Su, W. Cooperative hydrogen production and C-C coupling organic synthesis in one photoredox cycle. *Appl. Catal. B: Environ.* **2022**, 302, 120812.

(13) Kampouri, S.; Stylianou, K. C. Dual-functional photocatalysis for simultaneous hydrogen production and oxidation of organic substances. *ACS Catal.* **2019**, 9, 4247-4270.

(14) Niu, F.; Tu, W.; Lu, X.; Chi, H.; Zhu, H.; Zhu, X.; Wang, L.; Xiong, Y.; Yao, Y.; Zhou, Y.; Zou, Z. Single Pd-S_x sites in situ coordinated on CdS surface as efficient hydrogen autotransfer shuttles for highly selective visible-light-driven C-N coupling. *ACS Catal.* **2022**, 12, 4481-4490.

(15) Li, X.; Luo, Q.; Han, L.; Deng, F.; Yang, Y.; Dong, F. Enhanced photocatalytic degradation and H_2 evolution performance of N-CDs/S-C_3N_4 S-scheme heterojunction constructed by π-π conjugate self-assembly. *J. Mater. Sci. Technol.* **2022**, 114, 222-232.

(16) Luo, B.; Liu, G.; Wang, L. Recent advances in 2D materials for photocatalysis. *Nanoscale* **2016**, 8, 6904-6920.

(17) Tan, C.; Cao, X.; Wu, X.-J.; He, Q.; Yang, J.; Zhang, X.; Chen, J.; Zhao, W.; Han, S.; Nam, G.-H.; Sindoro, M.; Zhang, H. Recent advances in ultrathin two-dimensional nanomaterials. *Chem. Rev.* **2017**, 117, 6225-6331.

(18) Di, J.; Xiong, J.; Li, H.; Liu, Z. Ultrathin 2D photocatalysts: electronic-structure tailoring, hybridization, and applications. *Adv. Mater.* **2018**, 30, 1704548.

(19) Yang, R.; Mei, L.; Fan, Y.; Zhang, Q.; Zhu, R.; Amal, R.; Yin, Z.; Zeng, Z. $ZnIn_2S_4$-based photocatalysts for energy and environmental applications. *Small Methods* **2021**, 5, 2100887.

(20) Shi, X.; Dai, C.; Wang, X.; Hu, J.; Zhang, J.; Zheng, L.; Mao, L.; Zheng, H.; Zhu, M. Protruding Pt single-sites on hexagonal $ZnIn_2S_4$ to accelerate photocatalytic hydrogen evolution. *Nat. Commun.* **2022**, 13, 1287.

(21) Zhang, T.; Wang, T.; Meng, F.; Yang, M.; Kawi, S. Recent advances in $ZnIn_2S_4$-based materials towards photocatalytic purification, solar fuel production and organic transformations. *J. Mater. Chem. C* **2022**, 10, 5400-5424.

(22) Mei, Z.; Wang, G.; Yan, S.; Wang, J. Rapid microwave-assisted synthesis of 2D/1D $ZnIn_2S_4/TiO_2$ S-scheme heterojunction for catalyzing photocatalytic hydrogen evolution. *Acta Phys.-Chim. Sin.* **2021**, 37, 2009097.

(23) Li, X.; Lu, S.; Yi, J.; Shen, L.; Chen, Z.; Xue, H.; Qian, Q.; Yang, M.-Q. Ultrathin two-dimensional $ZnIn_2S_4/Ni_x$-B heterostructure for high-performance photocatalytic fine chemical synthesis and H_2 generation. *ACS Appl. Mater. Interfaces* **2022**, 14, 25297-25307.

(24) Xu, X. T.; Pan, L.; Zhang, X.; Wang, L.; Zou, J. J. Rational design and construction of cocatalysts for semiconductor-based photoelectrochemical oxygen evolution: a comprehensive review. *Adv. Sci.* **2019**, 6, 1801505.

(25) Yang, J.; Wang, D.; Han, H.; Li, C. Roles of cocatalysts in photocatalysis and photoelectrocatalysis. *Acc. Chem. Res.* **2013**, 46, 1900-1909.

(26) Xiao, N.; Li, S.; Li, X.; Ge, L.; Gao, Y.; Li, N. The roles and mechanism of cocatalysts in photocatalytic water splitting to produce hydrogen. *Chin. J. Catal.* **2020**, 41, 642-671.

(27) Zhong, S.; Xi, Y.; Wu, S.; Liu, Q.; Zhao, L.; Bai, S. Hybrid cocatalysts in semiconductor-based photocatalysis and photoelectrocatalysis. *J. Mater. Chem. A* **2020**, 8, 14863-14894.

(28) Jiao, L.; Dong, Y.; Xin, X.; Qin, L.; Lv, H. Facile integration of Ni-substituted polyoxometalate catalysts into mesoporous light-responsive metal-organic framework for effective photogeneration of hydrogen. *Appl. Catal. B: Environ.* **2021**, 291, 120091.

(29) Lu, S.; Weng, B.; Chen, A.; Li, X.; Huang, H.; Sun, X.; Feng, W.; Lei, Y.; Qian, Q.; Yang, M.-Q. Facet engineering of Pd nanocrystals for enhancing photocatalytic hydrogenation: modulation of the Schottky barrier height and enrichment of surface reactants. *ACS Appl. Mater. Interfaces* **2021**, 13, 13044-13054.

(30) Zhu, T.; Ye, X.; Zhang, Q.; Hui, Z.; Wang, X.; Chen, S. Efficient utilization of photogenerated electrons and holes for photocatalytic redox reactions using visible light-driven Au/$ZnIn_2S_4$ hybrid. *J. Hazard. Mater.* **2019**, 367, 277-285.

(31) Ouyang, W.; Muñoz-Batista, M. J.; Kubacka, A.; Luque, R.; Fernández-García, M. Enhancing photocatalytic performance of TiO_2 in H_2 evolution via Ru co-catalyst deposition. *Appl. Catal. B: Environ.* **2018**, 238, 434-443.

(32) Ran, J.; Zhang, J.; Yu, J.; Jaroniec, M.; Qiao, S. Z. Earth-abundant cocatalysts for semiconductor-based photocatalytic water splitting. *Chem. Soc. Rev.* **2014**, 43, 7787-7812.

(33) Li, X.; Li, M.; Liu, J.; Yi, J.; Yang, M.-Q.; Qian, Q. Amorphous nickel borate as a high-efficiency cocatalyst for H_2 generation and fine chemical synthesis. *Catal. Commun.* **2022**, 162, 106389.

(34) Zeng, D.; Zhou, T.; Ong, W.-J.; Wu, M.; Duan, X.; Xu, W.; Chen, Y.; Zhu, Y.-A.; Peng, D.-L. Sub-5 nm ultra-fine FeP nanodots as efficient co-catalysts modified porous g-C_3N_4 for precious-metal-free photocatalytic hydrogen evolution under visible light. *ACS Appl. Mater. Interfaces* **2019**, 11, 5651-5660.

(35) Shen, R.; Ding, Y.; Li, S.; Zhang, P.; Xiang, Q.; Ng, Y. H.; Li, X. Constructing low-cost Ni_3C/twin-crystal $Zn_{0.5}Cd_{0.5}S$ heterojunction/homojunction nanohybrids for efficient photocatalytic H_2 evolution. *Chin. J. Catal.* **2021**, 42, 25-36.

(36) Xiong, Z.; Hou, Y.; Yuan, R.; Ding, Z.; Ong, W.-J.; Wang, S. Hollow $NiCo_2S_4$ nanospheres as a cocatalyst to support $ZnIn_2S_4$ nanosheets for visible-light-driven hydrogen production. *Acta Phys.-Chim. Sin.* **2022**, 38, 2111021.

DOI: 10.14102/j.cnki.0254-5861.2022-0147

(37) Jiang, Z.; Chen, Q.; Zheng, Q.; Shen, R.; Zhang, P.; Li, X. Constructing 1D/2D Schottky-based heterojunctions between $Mn_{0.2}Cd_{0.8}S$ nanorods and Ti_3C_2 nanosheets for boosted photocatalytic H_2 evolution. *Acta Phys.-Chim. Sin.* **2021**, 37, 2010059.
(38) Qi, W.; Wang, C.; Yu, J.; Adimi, S.; Thomas, T.; Guo, H.; Liu, S.; Yang, M. MOF-derived porous ternary nickel iron nitride nanocube as a functional catalyst toward water splitting hydrogen evolution for solar to chemical energy conversion. *ACS Appl. Energy Mater.* **2022**, 5, 6155-6162.
(39) Cheng, Z.; Qi, W.; Pang, C. H.; Thomas, T.; Wu, T.; Liu, S.; Yang, M. Recent advances in transition metal nitride-based materials for photocatalytic applications. *Adv. Funct. Mater.* **2021**, 31, 2100553.
(40) Zheng, J.; Zhang, W.; Zhang, J.; Lv, M.; Li, S.; Song, H.; Cui, Z.; Du, L.; Liao, S. Recent advances in nanostructured transition metal nitrides for fuel cells. *J. Mater. Chem. A* **2020**, 8, 20803-20818.
(41) Wang, H.; Li, J.; Li, K.; Lin, Y.; Chen, J.; Gao, L.; Nicolosi, V.; Xiao, X.; Lee, J. M. Transition metal nitrides for electrochemical energy applications. *Chem. Soc. Rev.* **2021**, 50, 1354-1390.
(42) Xiang, Z.; Guan, H.; Zhang, B.; Zhao, Y. Electrostatic self-assembly of 2D-2D CoP/$ZnIn_2S_4$ nanosheets for efficient photocatalytic hydrogen evolution. *J. Am. Ceram. Soc.* **2020**, 104, 504-513.
(43) Yang, M.-Q.; Xu, Y.-J.; Lu, W.; Zeng, K.; Zhu, H.; Xu, Q.-H.; Ho, G. W. Self-surface charge exfoliation and electrostatically coordinated 2D hetero-layered hybrids. *Nat. Commun.* **2017**, 8, 14224.
(44) Luo, D.; Peng, L.; Wang, Y.; Lu, X.; Yang, C.; Xu, X.; Huang, Y.; Ni, Y. Highly efficient photocatalytic water splitting utilizing a WO_{3-x}/$ZnIn_2S_4$ ultrathin nanosheet Z-scheme catalyst. *J. Mater. Chem. A* **2021**, 9, 908-914.
(45) Zhu, Z.; Li, X.; Qu, Y.; Zhou, F.; Wang, Z.; Wang, W.; Zhao, C.; Wang, H.; Li, L.; Yao, Y. A hierarchical heterostructure of CdS QDs confined on 3D $ZnIn_2S_4$ with boosted charge transfer for photocatalytic CO_2 reduction. *Nano Res.* **2021**, 14, 81-90.
(46) Xu, W.; Tian, W.; Meng, L.; Cao, F.; Li, L. Interfacial chemical bond-modulated Z-scheme charge transfer for efficient photoelectrochemical water splitting. *Adv. Energy Mater.* **2021**, 11, 2003500.
(47) Li, H.; Ci, S.; Zhang, M.; Chen, J.; Lai, K.; Wen, Z. Facile spray-pyrolysis synthesis of yolk-shell earth-abundant elemental nickel-iron-based nanohybrid electrocatalysts for full water splitting. *ChemSusChem* **2017**, 10, 4756-4763.
(48) Liu, Z.; Tan, H.; Xin, J.; Duan, J.; Su, X.; Hao, P.; Xie, J.; Zhan, J.; Zhang, J.; Wang, J.-J.; Liu, H. Metallic intermediate phase inducing morphological transformation in thermal nitridation: Ni_3FeN-based three-dimensional hierarchical electrocatalyst for water splitting. *ACS Appl. Mater. Interfaces* **2018**, 10, 3699-3706.
(49) Jia, X.; Zhao, Y.; Chen, G.; Shang, L.; Shi, R.; Kang, X.; Waterhouse, G. I. N.; Wu, L.-Z.; Tung, C.-H.; Zhang, T. Ni_3FeN nanoparticles derived from ultrathin NiFe-layered double hydroxide nanosheets: an efficient overall water splitting electrocatalyst. *Adv. Energy Mater.* **2016**, 6, 1502585.
(50) Gu, Y.; Chen, S.; Ren, J.; Jia, Y. A.; Chen, C.; Komarneni, S.; Yang, D.; Yao, X. Electronic structure tuning in Ni_3FeN/r-GO aerogel toward bifunctional electrocatalyst for overall water splitting. *ACS Nano* **2018**, 12, 245-253.
(51) Li, Z.; Jang, H.; Qin, D.; Jiang, X.; Ji, X.; Kim, M. G.; Zhang, L.; Liu, X.; Cho, J. Alloy-strain-output induced lattice dislocation in Ni_3FeN/Ni_3Fe ultrathin nanosheets for highly efficient overall water splitting. *J. Mater. Chem. A* **2021**, 9, 4036-4043.
(52) Wang, X.; Wang, H.; Zhang, H.; Yu, W.; Wang, X.; Zhao, Y.; Zong, X.; Li, C. Dynamic interaction between methylammonium lead Iodide and TiO_2 nanocrystals leads to enhanced photocatalytic H_2 evolution from HI splitting. *ACS Energy Lett.* **2018**, 3, 1159-1164.
(53) Zhang, G.; Chen, D.; Li, N.; Xu, Q.; Li, H.; He, J.; Lu, J. Construction of hierarchical hollow Co_9S_8/$ZnIn_2S_4$ tubular heterostructures for highly efficient solar energy conversion and environmental remediation. *Angew. Chem. Int. Ed.* **2020**, 59, 8255-8261.
(54) Meng, X.; Qi, W.; Kuang, W.; Adimi, S.; Guo, H.; Thomas, T.; Liu, S.; Wang, Z.; Yang, M. Chromium-titanium nitride as an efficient co-catalyst for photocatalytic hydrogen production. *J. Mater. Chem. A* **2020**, 8, 15774-15781.
(55) Sun, Z.; Chen, H.; Zhang, L.; Lu, D.; Du, P. Enhanced photocatalytic H_2 production on cadmium sulfide photocatalysts using nickel nitride as a novel cocatalyst. *J. Mater. Chem. A* **2016**, 4, 13289-13295.
(56) Wang, S.; Guan, B. Y.; Lou, X. W. D. Construction of $ZnIn_2S_4$-In_2O_3 hierarchical tubular heterostructures for efficient CO_2 photoreduction. *J. Am. Chem. Soc.* **2018**, 140, 5037-5040.
(57) Makula, P.; Pacia, M.; Macyk, W. How to correctly determine the band gap energy of modified semiconductor photocatalysts based on UV-Vis spectra. *J. Phys. Chem. Lett.* **2018**, 9, 6814-6817.
(58) Niu, P.; Zhang, L.; Liu, G.; Cheng, H.-M. Graphene-like carbon nitride nanosheets for improved photocatalytic activities. *Adv. Funct. Mater.* **2012**, 22, 4763-4770.
(59) Prajapati, P. K.; Kumar, A.; Jain, S. L. First photocatalytic synthesis of cyclic carbonates from CO_2 and epoxides using CoPc/TiO_2 hybrid under mild conditions. *ACS Sustain. Chem. Eng.* **2018**, 6, 7799-7809.
(60) Li, X. l.; Wang, X. J.; Zhu, J. Y.; Li, Y. P.; Zhao, J.; Li, F. T. Fabrication of two-dimensional Ni_2P/$ZnIn_2S_4$ heterostructures for enhanced photocatalytic hydrogen evolution. *Chem. Eng. J.* **2018**, 353, 15-24.
(61) Xie, W.; Liu, L.; Cui, W.; An, W. Enhancement of photocatalytic activity under visible light irradiation via the AgI@TCNQ core-shell structure. *Materials* **2019**, 12, 1679.
(62) Liu, S.; Guo, Z.; Qian, X.; Zhang, J.; Liu, J.; Lin, J. Sonochemical deposition of ultrafine metallic Pt nanoparticles on CdS for efficient photocatalytic hydrogen evolution. *Sustain. Energy Fuels* **2019**, 3, 1048-1054.
(63) Zeng, D.; Lu, Z.; Gao, X.; Wu, B.; Ong, W.-J. Hierarchical flower-like $ZnIn_2S_4$ anchored with well-dispersed $Ni_{12}P_5$ nanoparticles for high-quantum-yield photocatalytic H_2 evolution under visible light. *Catal. Sci. Technol.* **2019**, 9, 4010-4016.
(64) Ng, S. W. L.; Gao, M.; Lu, W.; Hong, M.; Ho, G. W. Selective wavelength enhanced photochemical and photothermal H_2 generation of classical oxide supported metal catalyst. *Adv. Funct. Mater.* **2021**, 31, 2104750.
(65) Mei, F.; Li, Z.; Dai, K.; Zhang, J.; Liang, C. Step-scheme porous g-C_3N_4/$Zn_{0.2}Cd_{0.8}S$-DETA composites for efficient and stable photocatalytic H_2 production. *Chin. J. Catal.* **2020**, 41, 41-49.
(66) Li, M.-X.; Guan, R.-Q.; Li, J.-X.; Zhao, Z.; Zhang, J.-K.; Dong, C.-C.; Qi, Y.-F.; Zhai, H.-J. Performance and mechanism research of Au-HSTiO_2 on photocatalytic hydrogen production. *Chin. J. Struct. Chem.* **2020**, 39, 1437-1443.
(67) Zuo, G.; Wang, Y.; Teo, W. L.; Xie, A.; Guo, Y.; Dai, Y.; Zhou, W.; Jana, D.; Xian, Q.; Dong, W.; Zhao, Y. Ultrathin $ZnIn_2S_4$ nanosheets anchored on $Ti_3C_2T_X$ MXene for photocatalytic H_2 evolution. *Angew. Chem. Int. Ed.* **2020**, 59, 11287-11292.
(68) Chen, T.; Li, M.; Shen, L.; Roeffaers, M. B. J.; Weng, B.; Zhu, H.; Chen, Z.; Yu, D.; Pan, X.; Yang, M.-Q.; Qian, Q. Photocatalytic anaerobic oxidation of aromatic alcohols coupled with H_2 production over $CsPbBr_3$/GO-Pt catalysts. *Front. Chem.* **2022**, 10, 833784.

DOI: 10.14102/j.cnki.0254-5861.2022-0147

(69) Yu, Z.; Yang, K.; Yu, C.; Lu, K.; Huang, W.; Xu, L.; Zou, L.; Wang, S.; Chen, Z.; Hu, J.; Hou, Y.; Zhu, Y. Steering unit cell dipole and internal electric field by highly dispersed Er atoms embedded into NiO for efficient CO_2 photoreduction. *Adv. Funct. Mater.* **2022**, 32, 2111999.

(70) Lim, W. Y.; Wu, H.; Lim, Y.-F.; Ho, G. W. Facilitating the charge transfer of $ZnMoS_4$/CuS p-n heterojunctions through ZnO intercalation for efficient photocatalytic hydrogen generation. *J. Mater. Chem. A* **2018**, 6, 11416-11423.

(71) Liu, Q.; Wang, M.; He, Y.; Wang, X.; Su, W. Photochemical route for synthesizing Co-P alloy decorated $ZnIn_2S_4$ with enhanced photocatalytic H_2 production activity under visible light irradiation. *Nanoscale* **2018**, 10, 19100-19106.

(72) Ma, X.-W.; Lin, H.-F.; Li, Y.-Y.; Wang, L.; Pu, X.-P.; Yi, X.-J. Dramatically enhanced visible-light-responsive H_2 evolution of $Cd_{1-x}Zn_xS$ via the synergistic effect of Ni_2P and 1T/2H MoS_2 cocatalysts. *Chin. J. Struct. Chem.* **2021**, 40, 7-22.

(73) Han, S.; Li, B.; Huang, L.; Xi, H.; Ding, Z.; Long, J. Construction of $ZnIn_2S_4$-$CdIn_2S_4$ microspheres for efficient photocatalytic reduction of CO_2 with visible light. *Chin. J. Struct. Chem.* **2022**, 41, 2201007-2201013.

(74) Gong, H.; Hao, X.; Li, H.; Jin, Z. A novel materials manganese cadmium sulfide/cobalt nitride for efficiently photocatalytic hydrogen evolution. *J. Colloid Interf. Sci.* **2021**, 585, 217-228.

(75) Zhu, T.; Xiao, Y.; Ren, Y.; Zeng, W.; Pan, A.; Zheng, Y.; Liu, Q. Unusual formation of $CoS_{0.61}Se_{0.25}$ anion solid solution with sulfur defects to promote electrocatalytic water reduction. *ACS Appl. Energy Mater.* **2021**, 4, 2976-2982.

(76) Chen, Z.-H.; Li, Y.-H.; Qi, M.-Y.; Tang, Z.-R.; Xu, Y.-J. Benzyl alcohol oxidation and hydrogen generation over MoS_2/$ZnIn_2S_4$ composite photocatalyst. *Res. Chem. Intermed.* **2022**, 48, 1-12.

(77) Jiang, D.; Chen, X.; Zhang, Z.; Zhang, L.; Wang, Y.; Sun, Z.; Irfan, R. M.; Du, P. Highly efficient simultaneous hydrogen evolution and benzaldehyde production using cadmium sulfide nanorods decorated with small cobalt nanoparticles under visible light. *J. Catal.* **2018**, 357, 147-153.

(78) Sun, Y.; Xue, C.; Chen, L.; Li, Y.; Guo, S.; Shen, Y.; Dong, F.; Shao, G.; Zhang, P. Enhancement of interfacial charge transportation through construction of 2D-2D p-n heterojunctions in hierarchical 3D CNFs/MoS_2/$ZnIn_2S_4$ composites to enable high-efficiency photocatalytic hydrogen evolution. *Sol. RRL* **2020**, 5, 2000722.

(79) Shen, R.; Lu, X.; Zheng, Q.; Chen, Q.; Ng, Y. H.; Zhang, P.; Li, X. Tracking S-scheme charge transfer pathways in Mo_2C/CdS H_2-evolution photocatalysts. *Sol. RRL* **2021**, 5, 2100177.

(80) Low, J.; Dai, B.; Tong, T.; Jiang, C.; Yu, J. In situ irradiated X-ray photo- electron spectroscopy investigation on a direct Z-scheme TiO_2/CdS composite film photocatalyst. *Adv. Mater.* **2019**, 31, 1802981.

(81) Lai, L.; Xing, F.; Cheng, C.; Huang, C. Hierarchical 0D $NiSe_2$/2D $ZnIn_2S_4$ nanosheet-assembled microflowers for enhanced photocatalytic hydrogen evolution. *Adv. Mater. Interfaces* **2021**, 8, 2100052.

(82) Wood, A.; Giersig, M.; Mulvaney, P. Fermi level equilibration in quantum dot-metal nanojunctions. *J. Phys. Chem. B* **2001**, 105, 8810-8815.

(83) Jakob, M.; Levanon, H.; Kamat, P. V. Charge distribution between UV-irradiated TiO_2 and gold nanoparticles: determination of shift in the Fermi level. *Nano Lett.* **2003**, 3, 353-358.

(84) Subramanian, V.; Wolf, E. E.; Kamat, P. V. Catalysis with TiO_2/gold nanocomposites. Effect of metal particle size on the Fermi level equilibration. *J. Am. Chem. Soc.* **2004**, 126, 4943-4950.

Received: June 3, 2022
Accepted: July 23, 2022
Published online: July 28, 2022
Published: December 2, 2022

DOI: 10.14102/j.cnki.0254-5861.2022-0147